Ocean Modelling 124 (2018) 48–60

Contents lists available at ScienceDirect

Ocean Modelling

journal homepage: www.elsevier.com/locate/ocemod

Bottom boundary layer forced by finite amplitude long and short surface waves motions

H. Elsafty*, P. Lynett

Viterbi School of Engineering, University of Southern California, Los Angeles, CA 90089, USA

ARTICLE INFO

Keywords:
Multiple scale perturbation
Two oscillatory motions
Swell-solitary motions
σ-Coordinate
Bottom boundary layer

ABSTRACT

A multiple-scale perturbation approach is implemented to solve the Navier–Stokes equations while including bottom boundary layer effects under a single wave and under two interacting waves. In this approach, fluid velocities and the pressure field are decomposed into two components: a potential component and a rotational component. In this study, the two components are exist throughout the entire water column and each is scaled with appropriate length and time scales. A one-way coupling between the two components is implemented. The potential component is assumed to be known analytically or numerically a prior, and the rotational component is forced by the potential component. Through order of magnitude analysis, it is found that the leading-order coupling between the two components occurs through the vertical convective acceleration. It is shown that this coupling plays an important role in the bottom boundary layer behavior. Its effect on the results is discussed for different wave-forcing conditions: purely harmonic forcing and impurely harmonic forcing. The approach is then applied to derive the governing equations for the bottom boundary layer developed under two interacting wave motions. Both motions—the shorter and the longer wave—are decomposed into two components, potential and rotational, as it is done in the single wave. Test cases are presented wherein two different wave forcings are simulated: (1) two periodic oscillatory motions and (2) short waves interacting with a solitary wave. The analysis of the two periodic motions indicates that nonlinear effects in the rotational solution may be significant even though nonlinear effects are negligible in the potential forcing. The local differences in the rotational velocity due to the nonlinear vertical convection coupling term are found to be on the order of 30% of the maximum boundary layer velocity for the cases simulated in this paper. This difference is expected to increase with the increase in wave nonlinearity.

1. Introduction

Oscillatory bottom boundary layers have been extensively studied in the literature through experiments and numerical models. Experiments are often performed using an oscillating water tunnel for laminar and turbulent boundary layers (Riedel et al., 1972; Kamphuis, 1975; Jonsson and Carlsen, 1976; Sleath, 1987; Jensen et al., 1989). However, the oscillating tunnel does not represent the flow under dispersive wave conditions, where vertical velocity could play an important role in the vicinity of the bed. Other experiments are performed in wave flumes such as van Doorn (1981) and Mirfenderesk and Young (2003).

Numerical models have been developed to include the bottom boundary layer effects under wave propagation using different approaches. One approach is through incorporating extra terms into the governing equations. For example, Liu and Orfila (2004) and Liu (2006) account for boundary layer effects by including a convolution integral in the depth-integrated continuity equation and solving Boussinesq-type wave equations for laminar and turbulent boundary layer flows. Other approaches tend to solve two sets of models: one set for the flow kinematics inside the boundary layer and another for the flow kinematics outside the boundary layer. This approach suffers from the need to assume a boundary layer thickness before solving the problem. For example, Lee and Cheung (1999) obtain flow kinematics by solving Reynolds-averaged Navier–Stokes equations inside the viscous flow region and the Laplace equation outside the viscous flow region, while implementing fully nonlinear free surface boundary conditions. Gilbert et al. (2007) couple a Numerical Wave Tank (NWT) potential flow solver with a large eddy simulation solver and study the sediment transport over partially buried obstacles. Harris and Grilli (2012) state due to the limitation on the grid size used in the large-eddy simulation model, this type of coupling is efficient when simulating simple cases. Harris and Grilli (2012) couple an extended version of the Zang et al. (1994) model of the large-eddy simulation solver with a NWT and simulate velocity fields under any arbitrary finite-amplitude

* Corresponding author.
E-mail address: elsafty@usc.edu (H. Elsafty).

https://doi.org/10.1016/j.ocemod.2018.02.005
Received 26 October 2017; Received in revised form 5 February 2018; Accepted 22 February 2018
Available online 23 February 2018
1463-5003/

wave motion.

Other researchers have used direct numerical simulation (DNS) of the three-dimensional Navier–Stokes equations. This approach provides more accurate solutions but is numerically expensive. For instance, Lin and Zhang (2008) simulate laminar bottom boundary layers generated under various wave motions; including sinusoidal, Stokes, cnoidal, and solitary waves. Vittori and Blondeaux (2008) similarly use direct numerical simulation to predict turbulent bottom boundary layers generated under solitary waves.

Many of these solutions and models are either too sophisticated to implement or numerically very demanding for large, complex problems. The shallow water wave models that have been used extensively in the literature are considered to be good practical approximations to nonlinear wave hydrodynamics and coastal processes in the near-shore zone. However, these models lack an accurate way to include boundary layer effects and thus bottom shear stresses. Kim et al. (2009) derive depth-integrated Boussinesq-type wave equations from Navier–Stokes (NS) equations and includes bottom-induced turbulence. They retain integrated horizontal and vertical vorticity terms; however, the vertical profile of the shear stress has to be assumed *a priori*.

We aim to develop a practical, yet accurate approach including bottom boundary layer effects for complex near-shore environments with multiple wave components. The approach followed here in this study differs from the existing boundary layer theories in the order of the decomposition of the flow and the scaling. In this study, the decomposition of the flow is done before the scaling contrary to other theories where decomposition of the flow is done after the scaling, i.e. Liu and Orfila (2004) and Liu (2006). Also, there has been insufficient research on bottom boundary layers generated under interacting oscillatory motions, although this interaction commonly exists in near-shore zones. Therefore, a multiple-scale approach to include bottom boundary layer effects under two wave motions is investigated in this study. Each wave motion is decomposed into a potential component and a rotational component, where each component is distinctly scaled. The derived governing equations including bottom boundary layer effects under single wave motion are presented in Section 2, along with the development of the one-dimensional numerical model with σ-coordinate transformation. Section 3 covers the model validation and comparison to available experimental and numerical data. Section 4 outlines the derivation of the governing equations for two wave motions and the corresponding model results. The main conclusions and future recommendations are stated in Section 5.

2. Model derivation and governing equations for single oscillatory motion

The first step in deriving our equation set is to decompose the wave motion into two components: potential and rotational. The basis for this decomposition and eventual scaling is that the potential, irrotational component exists everywhere throughout the water column whereas the rotational motion exists strongly near the bottom and decreases with increasing distance from the bottom (in the absence of wind stresses). This decomposition is used to scale the vertical coordinate for each component. In addition, the time scale for each component could be different depending on the characteristics of the problem.

Therefore, the multiple-scale perturbation approach is used to derive the governing equations in this analysis. Two time scales are presented: a convective time scale that is used to scale the potential component and viscous time scale that is used to scale the rotational component. Consequently, the horizontal velocity, the vertical velocity, and the pressure for the two components are scaled differently as will be shown later in the paper.

One of the advantages of this decomposition is that it results in a numerically simpler set of equations for the rotational component while maintaining the interaction between the two components (rotational and potential) of the wave motion. The allowance of the rotational component to exist throughout the water column enables us to apply boundary conditions only at the bottom and water surface. Thus, there is no need to assume that the boundary layer thickness extends to infinity or diminishes at some ad-hoc depth. This approach overcomes the need to use different models for the flow kinematics inside and for outside of the boundary layer. Also, viscous effects are allowed to have the same order of magnitude as the dispersion effects, contrary to some previous models in which viscous effects are assumed to be weaker than dispersion and nonlinear effects (Liu and Orfila, 2004; Liu, 2006; Orfila et al., 2007).

2.1. Dimensionless governing equations

In this section, the propagation of an oscillatory wave train in a constant water depth h', surface elevation $\eta'(x', y', t')$, frequency ω, and wave amplitude a' is considered. The wave motion is decomposed into two components where the superscript p denotes the potential component and r denotes the rotational component. This decomposition is done before scaling the physical quantities, unlike other approaches, where wave motion is decomposed after scaling. The decomposition are given as

$$\begin{aligned} u' &= u'^{p} + u'^{r}, \\ w' &= w'^{p} + w'^{r}, \\ p' &= p'^{p} + p'^{r}. \end{aligned} \tag{1}$$

where the prime denotes dimensional variables. Substituting the previous decomposition into the governing equations gives: the continuity equation and the momentum equations in the x and z directions, respectively, are

$$\frac{\partial u^{p'}}{\partial x'} + \frac{\partial u^{r'}}{\partial x'} + \frac{\partial w^{p'}}{\partial z^{p'}} + \frac{\partial w^{r'}}{\partial z^{r'}} = 0. \tag{2}$$

$$\begin{aligned} &\frac{\partial u^{p'}}{\partial t^{p'}} + \frac{\partial u^{r'}}{\partial t^{r'}} + u^{p'}\frac{\partial u^{p'}}{\partial x'} + u^{p'}\frac{\partial u^{r'}}{\partial x'} + u^{r'}\frac{\partial u^{p'}}{\partial x'} + u^{r'}\frac{\partial u^{r'}}{\partial x'} + w^{p'}\frac{\partial u^{p'}}{\partial z^{p'}} + w^{p'}\frac{\partial u^{r'}}{\partial z^{r'}} \\ &\quad + w^{r'}\frac{\partial u^{p'}}{\partial z^{p'}} + w^{r'}\frac{\partial u^{r'}}{\partial z^{r'}} = -\frac{1}{\rho}\frac{\partial p^{p'}}{\partial x'} - \frac{1}{\rho}\frac{\partial p^{r'}}{\partial x'} + \nu'\frac{\partial^2 u^{p'}}{\partial x'^2} + \nu'\frac{\partial^2 u^{r'}}{\partial x'^2} + \nu'\frac{\partial^2 u^{p'}}{\partial z^{p'^2}} + \nu'\frac{\partial^2 u^{r'}}{\partial z^{r'^2}}, \end{aligned} \tag{3}$$

$$\begin{aligned} &\frac{\partial w^{p'}}{\partial t^{p'}} + \frac{\partial w^{r'}}{\partial t^{r'}} + u^{p'}\frac{\partial w^{p'}}{\partial x'} + u^{p'}\frac{\partial w^{r'}}{\partial x'} + u^{r'}\frac{\partial w^{p'}}{\partial x'} + u^{r'}\frac{\partial w^{r'}}{\partial x'} + w^{p'}\frac{\partial w^{p'}}{\partial z^{p'}} + w^{p'}\frac{\partial w^{r'}}{\partial z^{r'}} \\ &\quad + w^{r'}\frac{\partial w^{p'}}{\partial z^{p'}} + w^{r'}\frac{\partial w^{r'}}{\partial z^{r'}} = -\frac{1}{\rho}\frac{\partial p^{p'}}{\partial z^{p'}} - \frac{1}{\rho}\frac{\partial p^{r'}}{\partial z^{r'}} - g + \nu'\frac{\partial^2 w^{p'}}{\partial x'^2} + \nu'\frac{\partial^2 w^{r'}}{\partial x'^2} \\ &\quad + \nu'\frac{\partial^2 w^{p'}}{\partial z^{p'^2}} + \nu'\frac{\partial^2 w^{r'}}{\partial z^{r'^2}}. \end{aligned} \tag{4}$$

The governing equations are non-dimensionalized by choosing the appropriate length scale and time scale for each of the two components. Shallow water wave scaling is presumed for the potential component. The wavelength l' is used for the horizontal length scale. The water depth h' is used for the vertical length scale, and $l'/\sqrt{gh'}$ is used for the time scale.

For the rotational component, the wavelength l' is used for the horizontal length scale as with the potential component. The parameter

δ^* is defined as $\delta^* = \delta'/h'$, where δ' is the dimensional boundary layer thickness. The magnitude of δ^* goes from near zero in the very smooth bottom limit, to 1 in the limit when the boundary layer occupies the whole water column, i.e., for long waves or currents over rough bottoms. Other researchers have incorporated this parameter, δ^* , in their scaling. For example, Vittori and Blondeaux (2008) and Blondeaux and Vittori (2012) use the boundary layer thickness, defined as $\sqrt{2\nu'h'/\sqrt{gh'}}$, as a viscous length scale to scale the horizontal and vertical dimensions inside the bottom boundary layer. The horizontal rotational velocity is scaled by the friction velocity, u_*, as usually done in boundary layer flows. In this study, the friction velocity is represented by the bottom velocity U_b, multiplied by a parameter. The parameter is β_1 for the horizontal rotational velocity and β_2 for the vertical rotational velocity. The order of magnitude of these two parameters will be discussed. The rotational pressure is considered to be a dynamic pressure and hence connected to the velocity scaling. It is scaled by the square of the velocity and hence the parameter is β_1^2.

The time scale for the rotational component is taken to be the viscous time. This time scale is defined as length scale divided by viscosity, $(\delta^* h')^2/\nu'$. Where ν' is the kinematic viscosity in the case of the laminar boundary layer and the eddy viscosity in the case of turbulent boundary layer. As it is mentioned before the flow is decomposed into potential component and rotational component where the rotational component is driven by the potential component. However, the potential forcing has a convective time-scale that differs from the time-scale for rotational component which is taken to be the viscous time-scale in this study. The behavior of the rotational component is very much related to the viscosity and thus the use of the viscosity in the time-scale meant to represent the diffusion/viscous time-scale. Lastly, the pressure is scaled by the density multiplied by the wave amplitude and gravity for both the potential and the rotational components.

2.2. Derivation of the governing equations

The propagation of two-dimensional waves are considered, where the x axis is taken to be in the direction of wave propagation and the positive z axis points vertically upward with zero at the still water level. The following dimensionless variables are introduced:

$$\left.\begin{aligned}
&(x, y) = \frac{x', y'}{l'}, \qquad z^p = \frac{z'}{h'}, \qquad z^r = \frac{z'}{\delta^* h'},\\
&t^p = \frac{\sqrt{gh'}\,t'}{l'}, \qquad t^r = \frac{\nu' t^{r'}}{\delta^{*2} h'^2},\\
&(u^p, v^p) = \frac{u^{p'}}{\varepsilon\sqrt{gh'}}, \qquad (u^r, v^r) = \frac{u^{r'}}{\beta_1\varepsilon\sqrt{gh'}},\\
&w^p = \frac{w^{p'}}{\mu\varepsilon\sqrt{gh'}}, \qquad w^r = \frac{w^{r'}}{\beta_2\varepsilon\sqrt{gh'}},\\
&p^p = \frac{p^{p'}}{\rho g a'}, \qquad p^r = \frac{p^{r'}}{\beta_1^2\rho g a'}, \qquad \eta = \frac{\eta'}{h'},\\
&\varepsilon = \frac{a'}{h'}, \qquad \mu = \frac{h'}{l'},
\end{aligned}\right\} \tag{5}$$

where (x', y') are the horizontal axes, z' is the vertical axis measured from the still water level, t' is time, (u', v') are the horizontal velocities, w' is the vertical velocity, p' is the pressure, g is the gravitational acceleration and ρ is the fluid density. Three small dimensionless parameters are introduced; the dispersion parameter μ ,the nonlinearity parameter ϵ, and the viscous parameter $\delta = \delta'/l'$ representing the vertical-to-horizontal aspect ratio of the boundary layer length scales (viscous equivalent to μ).

The dimensionless continuity equation and the dimensionless momentum equations in the x and z directions, respectively, are then become,

$$\mu\varepsilon\frac{\partial u^p}{\partial x} + \beta_1\mu\varepsilon\frac{\partial u^r}{\partial x} + \mu\varepsilon\frac{\partial w^p}{\partial z^p} + \frac{\beta_2\varepsilon}{\delta^*}\frac{\partial w^r}{\partial z^r} = 0 \tag{6}$$

$$\begin{aligned}
&\mu\varepsilon\frac{\partial u^p}{\partial t^p} + \mu\varepsilon\beta_1\frac{\partial u^r}{\partial t^r} + \mu\varepsilon^2 u^p\frac{\partial u^p}{\partial x} + \mu\varepsilon^2\beta_1 u^p\frac{\partial u^r}{\partial x} + \varepsilon^2\beta_1\mu u^r\frac{\partial u^p}{\partial x}\\
&+ \beta_1^2\varepsilon^2\mu u^r\frac{\partial u^r}{\partial x}\\
&+ \mu\varepsilon^2 w^p\frac{\partial u^p}{\partial z^p} + \frac{\beta_1\mu\varepsilon^2}{\delta^*}w^p\frac{\partial u^r}{\partial z^r} + \beta_2\varepsilon^2 w^r\frac{\partial u^p}{\partial z^p} + \frac{\beta_1\beta_2\varepsilon^2}{\delta^*}w^r\frac{\partial u^r}{\partial z^r}\\
&= -\mu\varepsilon\frac{\partial p^p}{\partial x} - \mu\varepsilon\beta_1^2\frac{\partial p^r}{\partial x}\\
&+ \mu\delta^2\varepsilon\frac{\partial^2 u^p}{\partial x^2} + \beta_1\mu\delta^2\varepsilon\frac{\partial^2 u^r}{\partial x^2} + \frac{\varepsilon\delta^2}{\mu}\frac{\partial^2 u^p}{\partial z^{p2}} + \mu\varepsilon\beta_1\frac{\partial^2 u^r}{\partial z^{r2}},
\end{aligned} \tag{7}$$

$$\begin{aligned}
&\mu^2\varepsilon\frac{\partial w^p}{\partial t^p} + \beta_2\varepsilon\mu\frac{\partial w^r}{\partial t^r} + \mu^2\varepsilon^2 u^p\frac{\partial w^p}{\partial x} + \beta_2\mu\varepsilon^2 u^p\frac{\partial w^r}{\partial x} + \beta_1\mu^2\varepsilon^2 u^r\frac{\partial w^p}{\partial x}\\
&+ \beta_1\beta_2\mu\varepsilon^2 u^r\frac{\partial w^r}{\partial x}\\
&+ \varepsilon^2\mu^2 w^p\frac{\partial w^p}{\partial z^p} + \frac{\beta_2\mu\varepsilon^2}{\delta^*}w^p\frac{\partial w^r}{\partial z^r} + \beta_2\varepsilon^2\mu w^r\frac{\partial w^p}{\partial z^p} + \frac{\beta_2^2\varepsilon^2}{\delta^*}w^r\frac{\partial w^r}{\partial z^r}\\
&= -\varepsilon\frac{\partial p^p}{\partial z^p} - \varepsilon\frac{\beta_1^2}{\delta^*}\frac{\partial p^r}{\partial z^r} - 1\\
&+ \mu^2\varepsilon\delta^2\frac{\partial^2 w^p}{\partial x^2} + \beta_2\mu\varepsilon\delta^2\frac{\partial^2 w^r}{\partial x^2} + \varepsilon\delta^2\frac{\partial^2 w^p}{\partial z^{p^2}} + \beta_2\varepsilon\mu\frac{\partial^2 w^r}{\partial z^{r2}}.
\end{aligned} \tag{8}$$

The above dimensionless governing Eqs. (6)–(8) contain potential terms, rotational terms, and interaction terms between the potential and rotational components. A perturbation expansion of the following form is assumed:

$$\begin{aligned}
u &= (u_o^p + \mu^2 u_1^p + \mu^4 u_2^p + \ldots) + (u_o^r + \delta^2 u_1^r + \delta^4 u_2^r + \ldots),\\
w &= (w_o^p + \mu^2 w_1^p + \mu^4 w_2^p + \ldots) + (w_o^r + \delta^2 w_1^r + \delta^4 w_2^r + \ldots),\\
p &= (p_o^p + \mu^2 p_1^p + \mu^4 p_2^p + \ldots) + (p_o^r + \delta^2 p_1^r + \delta^4 p_2^r + \ldots).
\end{aligned} \tag{9}$$

where the dispersion parameter, μ^2, is used as the small parameter of perturbation for the potential component, and the viscous parameter ,δ^2, is used as the small parameter of perturbation for the rotational component. Substituting the above perturbation in the dimensionless governing equations and retaining the leading order terms, μ^2 and δ^2, for the potential and rotational components, the following dimensionless equations are obtained:

$$\frac{\partial u_o^p}{\partial x} + \beta_1\frac{\partial u_o^r}{\partial x} + \frac{\partial w_o^p}{\partial z^p} + \frac{\beta_2}{\delta^*\mu}\frac{\partial w_o^r}{\partial z^r} = O(\mu^4, \delta^4, \ldots), \tag{10}$$

$$\begin{aligned}
&\frac{\partial u_o^p}{\partial t^p} + \beta_1\frac{\partial u_o^r}{\partial t^r} + \varepsilon u_o^p\frac{\partial u_o^p}{\partial x} + \varepsilon\beta_1 u_o^p\frac{\partial u_o^r}{\partial x} + \varepsilon\beta_1 u_o^r\frac{\partial u_o^p}{\partial x} + \beta_1^2\varepsilon u_o^r\frac{\partial u_o^r}{\partial x}\\
&+ \varepsilon w_o^p\frac{\partial u_o^p}{\partial z^p}\\
&+\frac{\beta_1\varepsilon}{\delta^*}w_o^p\frac{\partial u_o^r}{\partial z^r} + \frac{\beta_2\varepsilon}{\mu}w_o^r\frac{\partial u_o^p}{\partial z^p} + \frac{\beta_1\beta_2\varepsilon}{\mu\delta^*}w_o^r\frac{\partial u_o^r}{\partial z^r}\\
&= -\frac{\partial p_o^p}{\partial x} - \beta_1^2\frac{\partial p_o^r}{\partial x} + \delta^2\frac{\partial^2 u_o^p}{\partial x^2}\\
&+ \beta_1\delta^2\frac{\partial^2 u_o^r}{\partial x^2} + \frac{\delta^2}{\mu^2}\frac{\partial^2 u_o^p}{\partial z^{p2}} + \beta_1\frac{\partial^2 u_o^r}{\partial z^{r2}} + O(\mu^4, \delta^4, \mu^2\delta^2, \ldots),
\end{aligned} \tag{11}$$

$$\mu^2\varepsilon\frac{\partial w_o^p}{\partial t^p} + \beta_2\varepsilon\mu\frac{\partial w_o^r}{\partial t^r} + \mu^2\varepsilon^2 u_o^p\frac{\partial w_o^p}{\partial x} + \beta_2\mu\varepsilon^2 u_o^p\frac{\partial w_o^r}{\partial x} + \beta_1\mu^2\varepsilon^2 u_o^r\frac{\partial w_o^p}{\partial x} + \beta_1\beta_2\mu\varepsilon^2 u_o^r\frac{\partial w_o^r}{\partial x} + \varepsilon^2\mu^2 w_o^p\frac{\partial w_o^p}{\partial z^p} + \frac{\beta_2\mu\varepsilon^2}{\delta^*}w_o^p\frac{\partial w_o^r}{\partial z^r} + \beta_2\varepsilon^2\mu w_o^r\frac{\partial w_o^p}{\partial z^p} + \frac{\beta_2^2\varepsilon^2}{\delta^*}w_o^r\frac{\partial w_o^r}{\partial z^r} = -\varepsilon\frac{\partial p_o^p}{\partial z^p} - \varepsilon\frac{\beta_1^2}{\delta^*}\frac{\partial p_o^r}{\partial z^r} - 1 + \mu^2\varepsilon\delta^2\frac{\partial^2 w_o^p}{\partial x^2} + \beta_2\mu\varepsilon\delta^2\frac{\partial^2 w_o^r}{\partial x^2} + \varepsilon\delta^2\frac{\partial^2 w_o^p}{\partial z^{p2}} + \beta_2\varepsilon\mu\frac{\partial^2 w_o^r}{\partial z^{r2}} + O(\mu^4, \delta^4, \mu^2\delta^2, \ldots). \tag{12}$$

The potential solution is then factored out from the continuity and the momentum equations. Hence, the following dimensionless governing equations contain the leading order terms of the rotational component in addition to some interaction terms of the potential and rotational components as follows

$$\frac{\partial u_o^r}{\partial x} + \frac{\beta_2}{\delta^*\mu\beta_1}\frac{\partial w_o^r}{\partial z^r} = 0 + O\left(\frac{\mu^2}{\beta_1}, \frac{\delta^2}{\beta_1}, \ldots\right), \tag{13}$$

$$\frac{\partial u_o^r}{\partial t^r} + \varepsilon u_o^p\frac{\partial u_o^r}{\partial x} + \varepsilon u_o^r\frac{\partial u_o^p}{\partial x} + \beta_1\varepsilon u_o^r\frac{\partial u_o^r}{\partial x} + \frac{\varepsilon}{\delta^*}w_o^p\frac{\partial u_o^r}{\partial z^r} + \frac{\varepsilon\beta_2}{\mu\beta_1}w_o^r\frac{\partial u_o^p}{\partial z^p} + \frac{\varepsilon\beta_2}{\mu\delta^*}w_o^r\frac{\partial u_o^r}{\partial z^r} = -\beta_1\frac{\partial p_o^r}{\partial x} + \delta^2\frac{\partial^2 u_o^r}{\partial x^2} + \frac{\partial^2 u_o^r}{\partial z^{r2}} + O\left(\frac{\mu^2}{\beta_1}, \frac{\delta^2}{\beta_1}, \ldots\right), \tag{14}$$

$$\frac{\partial w_o^r}{\partial t^r} + \varepsilon u_o^p\frac{\partial w_o^r}{\partial x} + \frac{\beta_1\varepsilon}{\beta_2}u_o^r\frac{\partial w_o^p}{\partial x} + \beta_1\varepsilon u_o^r\frac{\partial w_o^r}{\partial x} + \frac{\varepsilon}{\delta^*}w_o^p\frac{\partial w_o^r}{\partial z^r} + \varepsilon w_o^r\frac{\partial w_o^p}{\partial z^p} + \frac{\beta_2\varepsilon}{\mu\delta^*}w_o^r\frac{\partial w_o^r}{\partial z^r} = -\frac{\beta_1^2}{\mu\beta_2\delta^*}\frac{\partial p_o^r}{\partial z^r} + \delta^2\frac{\partial^2 w_o^r}{\partial x^2} + \frac{\partial^2 w_o^r}{\partial z^{r2}} + O\left(\frac{\mu^2}{\varepsilon\mu\beta_2}, \frac{\delta^2}{\varepsilon\mu\beta_2}, \ldots\right). \tag{15}$$

2.3. The estimation of the order of magnitude for the small parameters β_1 and β_2

The leading order solution for the rotational component will depend on the order of magnitude of parameters $\beta_1 and \beta_2$. The order of magnitude for the parameter β_2 can be estimated by looking at the continuity Eq. (13). For the two dimensional problem, the two gradient terms must balance, such that $O(\beta_2) = O(\delta^*\mu\beta_1)$. Hence the two parameters are related.

The order of magnitude for the parameter β_1 can be estimated. The velocity scale $\beta_1\varepsilon\sqrt{gh'}$ approximates the friction velocity, u_* which it is usually represented as a function of the maximum bottom shear stress and/or the maximum bottom particle velocity. For example, friction velocity can be given as $u_*^2 = \tau_{bmax}/\rho = \frac{1}{2}f_w U_b^2$ where f_w is the friction factor, τ_{bmax} is the maximum bottom shear stress, and U_b is the maximum bottom particle velocity. In this paper, the friction velocity is represented as a function of the maximum bottom particle velocity U_b multiplied by the parameter β_1 where $u_* = \beta_1 U_b$. Applying the previous relations and with simple manipulations, the order of magnitude of the parameter, β_1, is found to be proportional to the square root of the friction factor f_w. Therefore, the order of magnitude for β_1 will depend on the characteristics of the problem under investigation.

The friction factor is often assumed to be a function of the Reynolds number and the bottom surface characteristics (smooth or rough) (e.g. Cox et al., 1996). For laminar bottom boundary layers, there are various methods to calculate the friction factor. For example, Nielsen (1992) uses the maximum bottom shear stress defined as, $\tau_{bmax} = \rho\sqrt{\nu\omega}\,U_b$, to obtain friction factor defined as, $f_w = 2\sqrt{\rho\omega}/U_b$. Mirfenderesk and Young (2003) represents the friction factor as a function of the Reynolds number, $f_w = 2/\sqrt{R_e}$, where the Reynolds number is calculated as, $R_e = A_b U_b/\nu$, with A_b is the maximum particle excursion at the bottom. Here, the definition for the friction factor will be used (Mirfenderesk and Young, 2003). Therefore, a typical value for the parameter β_1 in a laminar boundary layer would be in the range of O (0.01–0.1). In turbulent boundary layer, the above analysis will need further investigation.

3. Numerical model and results

A one-dimensional numerical model is developed to solve the governing equations for the rotational component. This numerical model will be called the viscous-sigma-model in this paper. The σ-coordinate transformation is applied in the vertical direction to ensure fine resolution near the bottom to properly resolve the boundary layer. The following transformation is implemented:

$$\sigma = \left(\frac{z+h}{h+\eta}\right)^{1/n}, \tag{16}$$

where n is a free power used to adjust the resolution of the numerical grid. We used a value of $n = 2$ as this provided acceptable resolution near the bottom yielding numerical convergent results. Before applying the viscous-sigma-model the leading order solution for the rotational component is found. This step requires an estimate of the relative order of magnitude of the parameter, β_1, and the other small parameters, μ, δ^*, and ϵ. From the x-momentum Eq. (14), the local acceleration term and the diffusion term are of the same order of magnitude. It is also noticed that the coupling term $w_o^p(u_o^r)_z$, with the coefficient $\frac{\varepsilon}{\delta^*}$, could have a comparable order of magnitude to both the local acceleration and the diffusion terms when $O(\delta^*)$ has the same order of magnitude as ϵ. The other terms in the x-momentum Eq. (14) have a higher order of magnitude and thus will be neglected in this study.

In this study, the coupling term, $w_o^p(u_o^r)_z$, is examined to quantify its effect on the bottom boundary layer behavior under various wave forcing types, including purely harmonic forcing, (i.e., oscillatory waves), and transient forcing, (i.e., solitary waves). Numerical calculations of the boundary layer are performed by specifying the potential component as an input to the viscous-sigma-model. The numerical simulation is run twice for each forcing type. In the first simulation, the horizontal momentum equation is solved without the coupling term, $w_o^p(u_o^r)_z$. The horizontal rotational velocity is obtained via solving the x-momentum Eq. (18), and it will be called the linear model solution. In the second simulation, the coupling term is retained. The horizontal rotational velocity is obtained via solving the x-momentum Eq. (19), and it will be called the nonlinear model solution. The two solutions will be plotted against experimental data to investigate the effect of this coupling term

The dimensional continuity, the x-momentum governing equations, and the boundary conditions for the rotational motion are,

$$\frac{\partial u^r}{\partial x} + \frac{\partial w^r}{\partial z^r} = 0, \tag{17}$$

$$\frac{\partial u^r}{\partial t^r} = \frac{\partial^2 u^r}{\partial z^{r2}}, \tag{18}$$

$$\frac{\partial u^r}{\partial t^r} + w^p\frac{\partial u^r}{\partial z^r} = \frac{\partial^2 u^r}{\partial z^{r2}}. \tag{19}$$

The no-slip boundary condition at the bottom and zero shear stress is assumed at the water surface:

$$u^r = -u^p \quad \text{at} \quad z = -h, \tag{20}$$

$$\frac{\partial u^r}{\partial z^r} = 0 \quad \text{at} \quad z = 0. \tag{21}$$

It is clear that the developed scaling in this study produces a simple solution for obtaining the rotational velocity component where only the vertical and time dimensions are required to solve the equations. The needed quantities to solve the above equations are the horizontal potential velocity at the bottom along with the vertical profile of the vertical potential velocity.

3.1. Oscillatory wave

The first set of simulations examines the boundary layer generated under oscillatory wave motion. Linear wave theory is used to provide the potential component in this case. The model results are compared to the experimental data of Mirfenderesk and Young (2003) for case S1, and the linear analytical solution by Lamb (1932). The Lamb (1932) solution for the total horizontal velocity is given as

$$u = u_m(\cos(kx - \omega t) - \exp(-\beta z)\cos(kx - \omega t + \beta z)), \quad (22)$$

where u_m is the maximum horizontal velocity near the bottom, k is the wave number, $\beta = \sqrt{\left(\frac{\omega}{2\nu}\right)}$ is the boundary layer parameter, and z is the distance from the bottom.

The single harmonic wave characteristics used in the experiment are: wave height of 0.12 m, wave period of 2 s, wavelength of 4.21 m, and a constant water depth of 0.55 m. The values of μ and ϵ are 0.13 and 0.11, respectively. The mesh in the viscous-sigma-model computational domain is composed of 201 grid points in the vertical direction with minimum $\Delta z = 1.5e-005$ m near the bottom. A constant time step of $\Delta t = 0.0001$ s is used. The simulation is run for 30 wave periods to ensure a fully developed boundary layer. The comparison of the model result with the experimental data and the analytical solution of Lamb (1932) are shown in Fig. (1). Only the accelerating phase is shown here. As is shown in the figure, the linear model results agree very well with the analytical solution of Lamb (1932). However, the nonlinear model results provide a better match to the experimental data. An explanation for this remark could be due to the weakly nonlinear nature of this configuration. The ratio $\frac{\varepsilon}{\delta^*}$ is of order $O(1)$ in this case further indicating that the coupling term is important, and likely influences the solution.

The second oscillatory data set used for comparison is the numerical solution of the three-dimensional Navier–Stokes equations by Lin and Zhang (2008). In this case, the wave height is 0.01 m, the wave period of 3 s, and the wave propagates in a constant water depth of 1.0 m, ($\varepsilon = 0.005$ and $\mu = 0.1$). 201 grid points are used in the vertical direction with minimum $\Delta z = 2.5e-005$ m near the bottom. The model is run for 30 wave periods with a constant time step of $\Delta t = 0.0001$ s. In this case, both the linear and nonlinear model results agree very well with the numerical results of Lin and Zhang (2008) as shown in Fig. (2). In this case, $\frac{\varepsilon}{\delta^*}$ is less than $O(1)$. Thus, the effect of the coupling term in this test case is small compared to the previous data set. It is worth noting that the computational cost for running our model is much less than the full three dimensional model of Lin and Zhang (2008) while obtaining the same accuracy.

3.2. Solitary wave

The next set of simulations examines the boundary layer generated under solitary waves. In these simulations, the potential component is

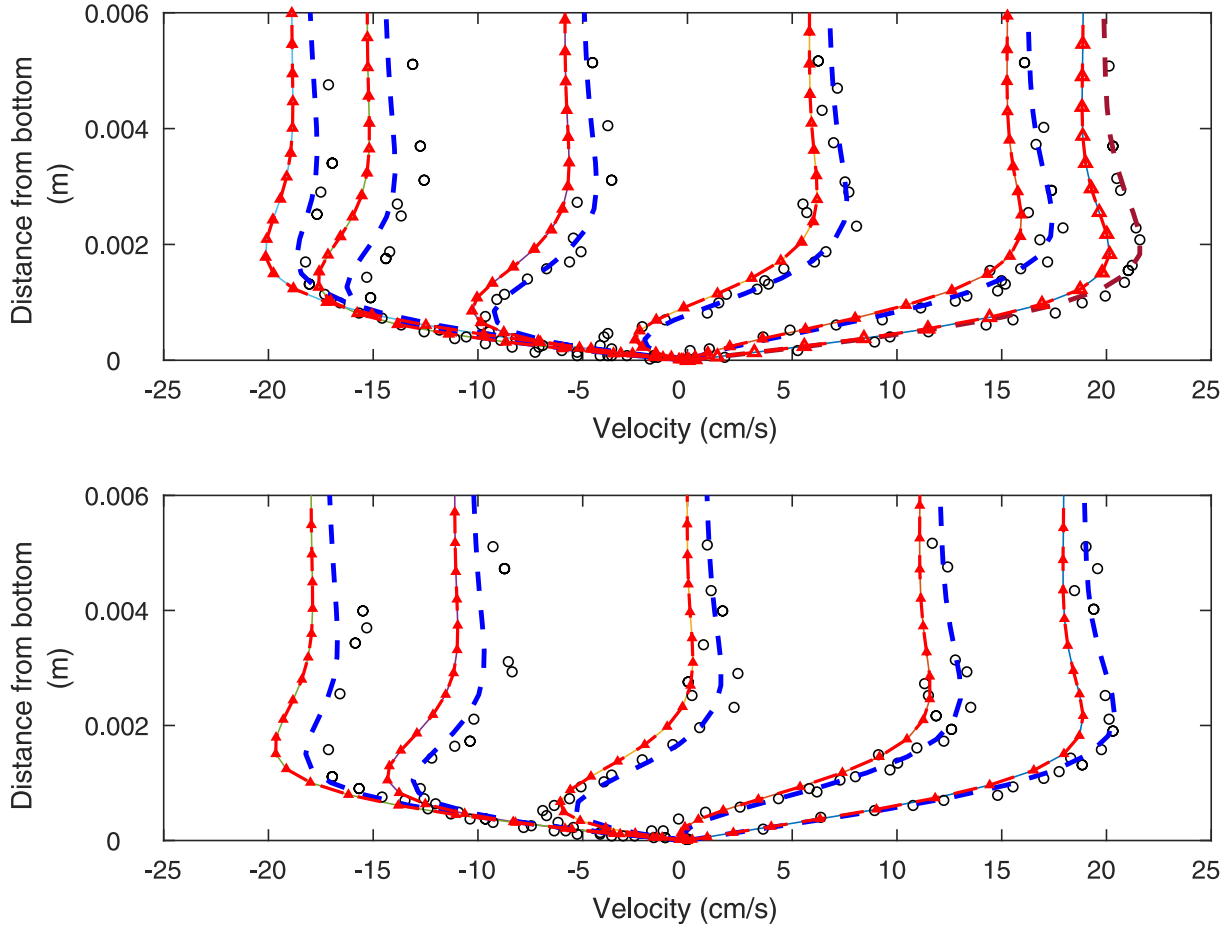

Fig. 1. Vertical profiles of the horizontal velocity in the laminar boundary layer under a linear wave at $\omega t = 0°, 36°, 72°, 108°, 144°$, and $180°$ (top) and at $\omega t = 18°, 54°, 90°, 126°$, and $162°$ (bottom) from right to left, respectively. Solid line: linear numerical model; dashed line: nonlinear numerical model; Δ: analytical solution; ○: experimental data of Mirfenderesk and Young (2003).

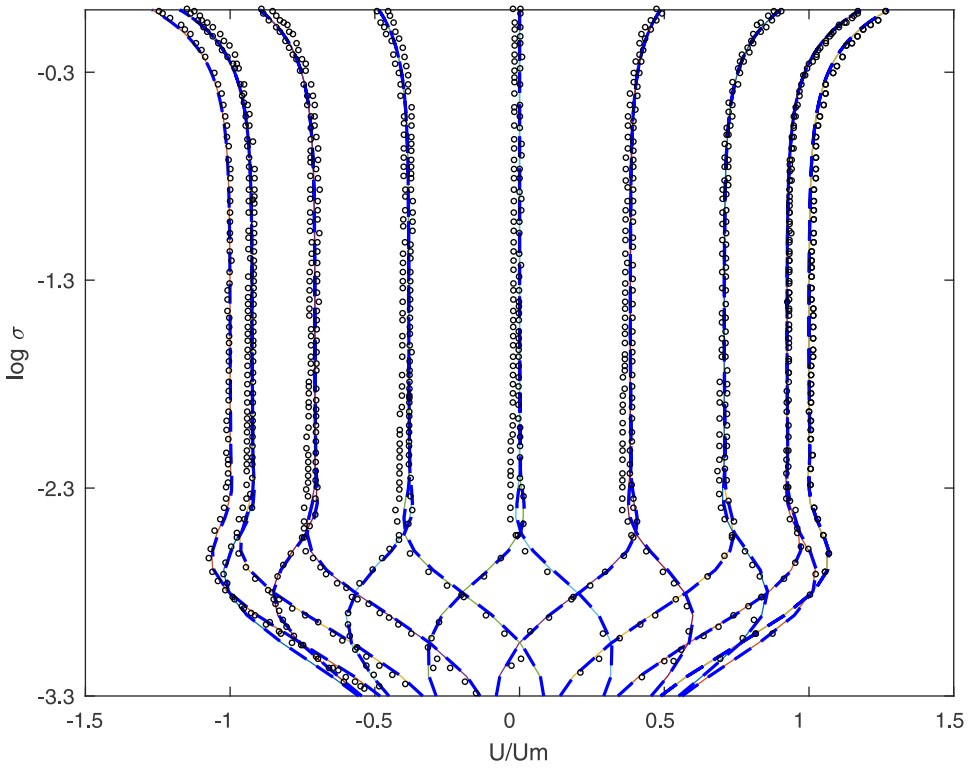

Fig. 2. Vertical profiles of the horizontal velocity in the laminar boundary layer under a linear wave at $\omega t = n\pi/8$ ($n = 0, 1, 2, \cdots, 16$). Solid line: linear numerical model; dashed line: nonlinear numerical model (overlays solid line closely); ○: numerical solution from Lin and Zhang (2008).

numerically obtained by solving the one-dimensional Boussinesq-type wave model of Lynett and Liu (2002). The dimensional continuity equation and the horizontal momentum equation are,

$$\frac{\partial \eta}{\partial t} + \frac{\partial}{\partial x}(h+\eta)u_\alpha - \frac{\partial}{\partial x}\left\{(h+\eta)\left[\left(\frac{h^2}{6} - \frac{1}{2}z_\alpha^2\right)\frac{\partial u_\alpha}{\partial x} + \left(\frac{1}{2}(\eta - h) - z_\alpha\right)\frac{\partial (hu_\alpha)/\partial x}{\partial x}\right]\right\} = 0 \tag{23}$$

$$\frac{\partial u_\alpha}{\partial t} + \frac{1}{2}\frac{\partial u_\alpha^2}{\partial x} + g\frac{\partial \eta}{\partial x} + \frac{\partial}{\partial t}\left\{\frac{1}{2}z_\alpha^2\frac{\partial u_\alpha}{\partial x} + z_\alpha\frac{\partial (hu_\alpha)/\partial x}{\partial x}\right\} = 0, \tag{24}$$

where u_α is the velocity at the reference level, z_α, and is taken as -0.531h, Nwogu (1993). The vertical profiles for the horizontal and vertical velocities are obtained via the equations

$$u = u_\alpha - \frac{1}{2}(z^2 - z_\alpha^2)u_{\alpha xx} - (z - z_\alpha)(hu_\alpha)_{xx}, \tag{25}$$

$$w = -z_\alpha u_{\alpha x} - (hu_\alpha)_x. \tag{26}$$

An Adams–Bashforth–Moulton predictor–corrector scheme is used to integrate the continuity Eq. (23) and the x-momentum Eq. (24). The potential horizontal and vertical velocities are obtained along with the surface elevation and both are passed to the viscous-sigma-model. Finally, the potential component is added to the rotational component to obtain the total velocity field.

Two data sets of the experiment done by Liu et al. (2007) are used for comparison. The first set uses a water depth of 0.1 m, and a solitary wave height of 0.02 m. The dispersion and the nonlinearity parameters, ϵ and μ, are 0.2 and 0.0658, respectively. The computational domain of the one-dimensional Boussinesq model consists of 7000 grid points in the x direction with $\Delta x = 0.001$ m. The viscous-sigma-model has 201 grid points in the vertical direction with minimum $\Delta z = 2.5e-006$ m near the bottom. A constant time step of $\Delta t = 3e-005$ s is used.

First, the numerical solution is compared with the experimental data. Both linear and nonlinear solutions of the viscous-sigma-model are obtained. In general, both solutions agree well with the experimental data in the accelerating phase. However, a remarkable difference between the linear solution and the nonlinear solution in the decelerating phase is noticed, as shown in Fig. (3). The results of the nonlinear model show better agreement with the experimental data in the decelerating phase. The coupling term in the x-momentum equation is presumed to have an effect in the decelerating phase. It is also noticed that the computational time for the linear model and the nonlinear model are very close as the vertical potential velocity is known.

Bottom shear stresses are calculated using the rotational velocity gradient at the bottom and are shown in Fig. (4). The calculated bottom shear stresses agree with both the experimental results and the analytical solution of Liu et al. (2007). The change in sign in the bottom shear stress is captured by the model results, even though the velocity outside the boundary layer is always in the direction of the wave propagation. There are very small differences between the bottom shear stress computed from the linear and the nonlinear model and the comparison has been separated in two plots for clearness. This result suggests our approach is an accurate and practical way for calculating bottom shear stress compared to, for example, the quadratic drag law driven by the bottom potential velocity.

The characteristics of the second data set of Liu et al. (2007) are: water depth of 0.1 m, and wave height of 0.03 with ϵ and μ equal 0.3 and 0.0813, respectively. The viscous-sigma-model has 201 grid points in the vertical direction with minimum $\Delta z = 2.5e-006$ m near the bottom and a constant time step of $\Delta t = 3.4e-005$ s. The comparison with the experimental data is shown in Fig. (5). Both the linear and nonlinear model solutions are able to predict the velocity profile in the accelerating phase with the tendency of the nonlinear solution to better match the experimental data in the decelerating phase.

Bottom shear stress is calculated and compared with the experimental solitary wave data set $\varepsilon = 0.2$ to investigate the effect of wave nonlinearity. Decreasing shear stress with increasing wave nonlinearity, ϵ, is clear in Fig. (6), this is shown Liu et al. (2007) as well. The top

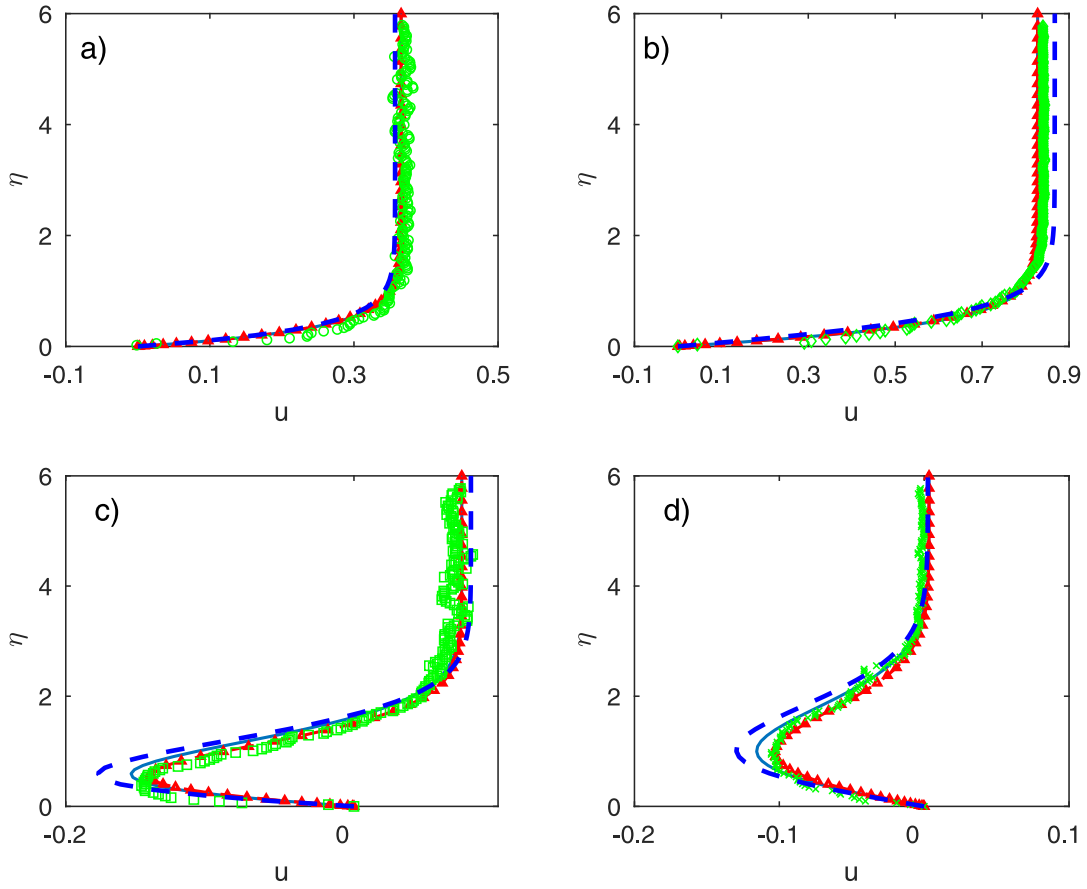

Fig. 3. Vertical profiles of the dimensionless horizontal velocity for $\epsilon = 0.2$. Solid line: linear model solution; – Δ–: nonlinear model; dashed line: numerical solution of the nonlinear boundary layer equation of Park (2009). Experimental data are denoted as follows: top accelerating phases, (a)-$\xi = -0.2$ ○; (b)- $\xi = -0.01$ ⋄; and bottom decelerating phases, (c)- $\xi = 0.37$ □; (d)-* $\xi = 0.70$ from Park (2009).

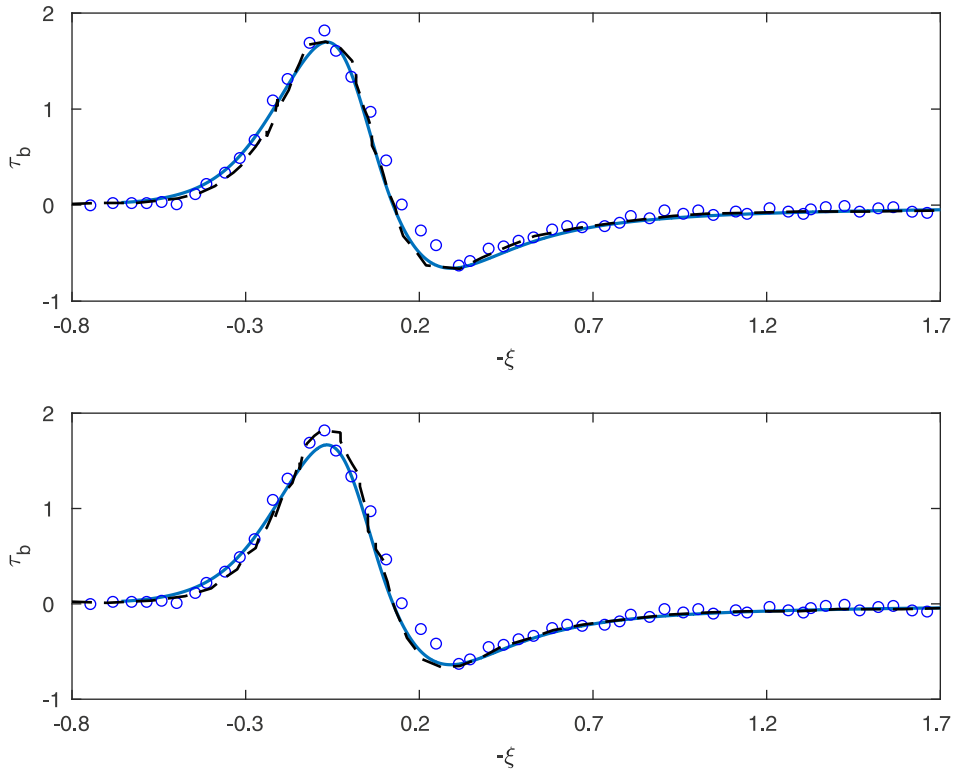

Fig. 4. Time history of the dimensionless bottom bed shear stress for $\varepsilon = 0.2$. Top figure solid line: linear model solution; dashed line: linear solution of Liu et al. (2007); ○: Experimental data of Liu et al. (2007); and bottom figure solid line: the nonlinear model; dashed line: nonlinear solution of Liu et al. (2007);○: Experimental data of Liu et al. (2007).

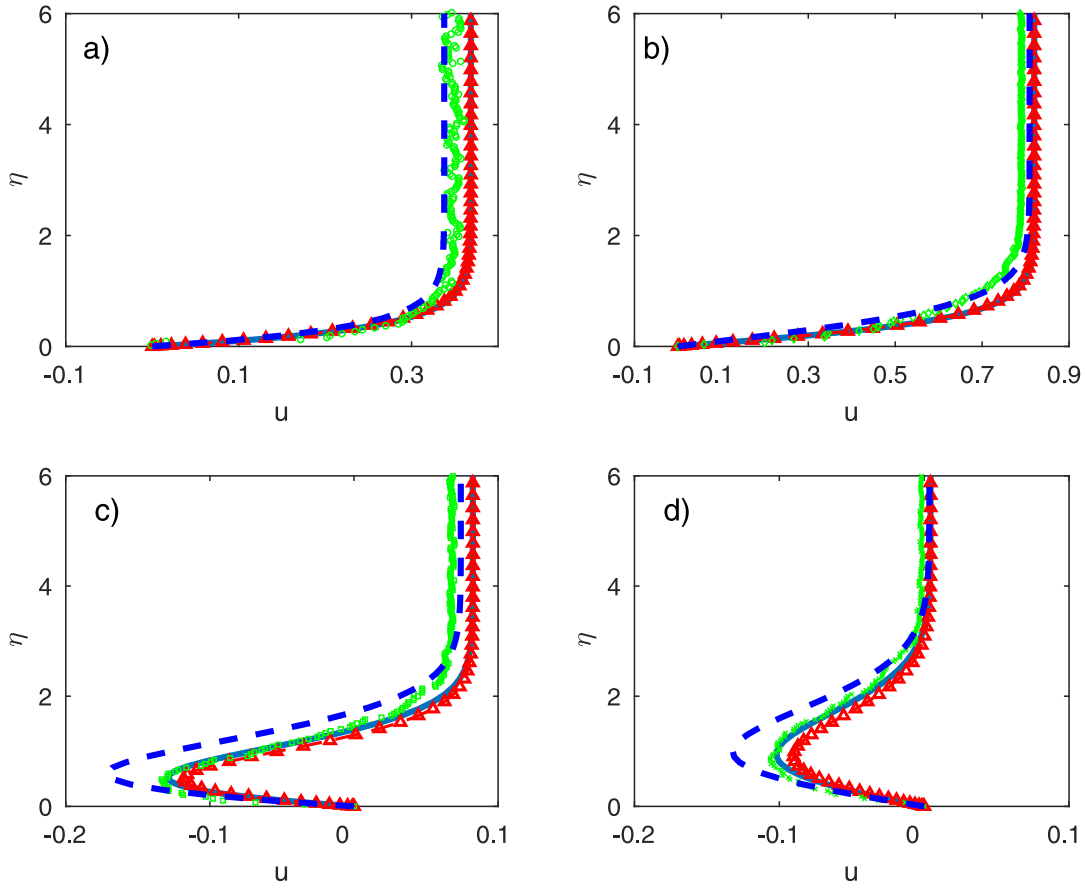

Fig. 5. Vertical profiles of the dimensionless horizontal velocity for ε = 0.3. Solid line: linear model solution; – Δ–: nonlinear model; dashed line: numerical solution of the nonlinear boundary layer equation of Park (2009). Experimental data are denoted as follows: top accelerating phases, (a)-$\xi = -0.22$ ○; (b)- $\xi = -0.03$ ⋄; and bottom decelerating phases, (c)-$\xi = 0.39$ □; (d)-$\xi = 0.70$ * from Park (2009).

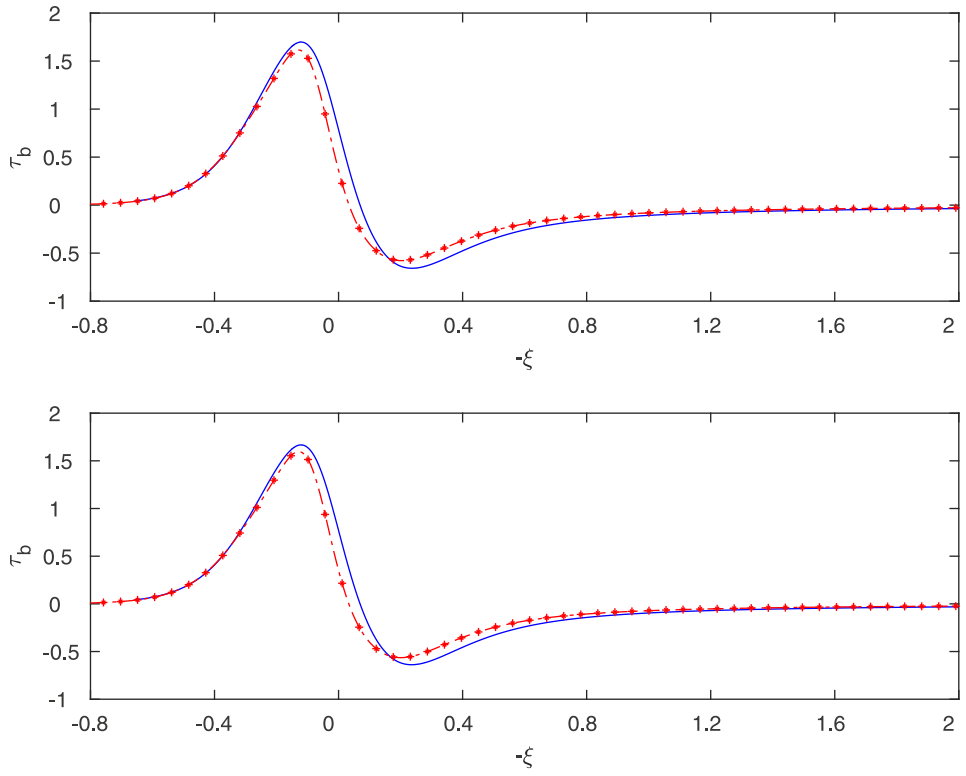

Fig. 6. Dimensionless bed shear stress for different values of nonlinearity: linear model in top figure and nonlinear model in bottom figure. Top figure: solid line for ε = 0.2 and dashed-line-circle for ε = 0.3. Bottom figure: solid line for ε = 0.2 and dashed-line-circle for ε = 0.3.

panel in Fig. 6 shows the comparison of bottom shear stress calculated using the linear model for $\epsilon = 0.2$ and $\epsilon = 0.3$. The bottom panel in the figure shows the comparison of bottom shear stress calculated using the nonlinear model for $\epsilon = 0.2$ and $\epsilon = 0.3$. Vittori and Blondeaux (2008) mention that for small amplitude waves, the boundary layer tends to remain laminar and the negative velocities during the flow reversal in the decelerating phase persist. They show that the flow reversal intensity and time duration decreases with increase in ϵ. The same properties are evident here while comparing the experiment data sets with the numerical solutions.

4. Model derivation and governing equations for two wave motions

In this section, the propagation of a wave train in a constant water depth is considered. The shorter wave motion has a surface elevation of $\eta_s'(x', y', t')$, a frequency ω_s, and a wave amplitude a_s' interacting with a longer wave motion that has a surface elevation of $\eta_l'(x', y', t')$, a frequency ω_l, and a wave amplitude a_l'. The decomposition of each wave motion of the two interacting waves into potential and rotational components is done here. The governing equations are non-dimensionalized by the appropriate length and time scales for each component of each wave. The following decomposition is used:

$$\begin{aligned}
u_s' &= u_s^{,p} + u_s^{,r}, \qquad u_l' = u_l^{,p} + u_l^{,r},\\
w_s' &= w_s^{,p} + w_s^{,r}, \qquad w_l' = w_l^{,p} + w_l^{,r},\\
p_s' &= p_s^{,p} + p_s^{,r}, \qquad p_l' = p_l^{,p} + p_l^{,r},
\end{aligned} \tag{27}$$

where the prime denotes dimensional variables. The superscript p denotes the potential component and r denotes the rotational component. The superscript s denotes the shorter wave and l denotes the longer wave. The following normalizations are used,

$$\left.\begin{aligned}
&(x_{s,l}, y_{s,l}) = \frac{x_{s,l}', y_{s,l}'}{l_{s,l}'}, \qquad z^p = \frac{z^{p'}}{h'}, \qquad z^r = \frac{z^{r'}}{\delta_{s,l}^* h'},\\
&t^p = \frac{\sqrt{gh'}\, t_{s,l}^{p'}}{l_{s,l}'}, \qquad t_{s,l}^r = \frac{\nu' t_{s,l}^{r'}}{\delta_{s,l}^{*2} h'^2}, \qquad \eta_{s,l} = \frac{\eta_{s,l}'}{h'},\\
&(u_{s,l}^p, v_{s,l}^p) = \frac{u_{s,l}^{p'}}{\epsilon_{s,l}\sqrt{gh'}}, \qquad (u_{s,l}^r, v_{s,l}^r) = \frac{u_{s,l}^{r'}}{\beta_{1s,1l}\epsilon_{s,l}\sqrt{gh'}},\\
&w_{s,l}^p = \frac{w_{s,l}^{p'}}{\mu_{s,l}\epsilon_{s,l}\sqrt{gh'}}, \qquad w_{s,l}^r = \frac{w_{s,l}^{r'}}{\beta_{2s,2l}\epsilon_{s,l}\sqrt{gh'}},\\
&p_{s,l}^p = \frac{p_{s,l}^{p'}}{\rho g a_{s,l}'}, \qquad p_{s,l}^r = \frac{p_{s,l}^{r'}}{\beta_1^2 \rho g a_{s,l}'}, \qquad \delta_{s,l}^2 = \frac{\nu'}{l_{s,l}'\sqrt{gh'}},\\
&\mu_{s,l} = \frac{h'}{l_{s,l}'}, \qquad \epsilon_{s,l} = \frac{a_{s,l}'}{h'}, \qquad \delta_{s,l} = \frac{\delta_{s,l}'}{l_{s,l}'}, \qquad \delta_{s,l}^* = \frac{\delta_{s,l}'}{h'}.
\end{aligned}\right\} \tag{28}$$

where $(x_{s,l}', y_{s,l}')$ are the horizontal axes, z' is the vertical axis measured from the still water level, $t_{s,l}'$ is time, $(u_{s,l}', v_{s,l}')$ are the horizontal velocities, $w_{s,l}'$ is the vertical velocity, is the pressure, g is the gravitational acceleration, and ρ is density. Six dimensionless small parameters are introduced: the dispersion parameters $\mu_{s,\,l}$, the viscous parameters $\delta_{s,\,l}$, and the nonlinearity parameters $\epsilon_{s,\,l}$. By substituting the previous decomposition relations and scaling into the governing equations, the dimensionless continuity equation and the dimensionless momentum equations in the x and z directions are, respectively,

$$a_1\frac{\partial u_s^p}{\partial x_s} + a_2\frac{\partial u_l^p}{\partial x_l} + a_1\beta_{1s}\frac{\partial u_s^r}{\partial x_s} + a_2\beta_{1l}\frac{\partial u_l^r}{\partial x_l} + a_1\frac{\partial w_s^p}{\partial z^p} + a_2\frac{\partial w_l^p}{\partial z^p} + a_3\frac{\partial w_s^r}{\partial z_s^r} + a_4\frac{\partial w_l^r}{\partial z_l^r} = 0 \tag{29}$$

$$\begin{aligned}
&a_1\frac{\partial u_s^p}{\partial t_s^p} + a_2\frac{\partial u_l^p}{\partial t_l^p} + a_1\beta_{1s}\frac{\partial u_s^r}{\partial t_s^r} + a_2\beta_{1l}\frac{\partial u_l^r}{\partial t_l^r} + a_5 u_s^p\frac{\partial u_s^p}{\partial x_s} + a_5\beta_{1s}u_s^p\frac{\partial u_s^r}{\partial x_s}\\
&+ a_5\beta_{1s}u_s^r\frac{\partial u_s^p}{\partial x_s} + a_5\beta_{1s}^2u_s^r\frac{\partial u_s^r}{\partial x_s} + a_7u_l^p\frac{\partial u_s^p}{\partial x_s} + a_7\beta_{1s}u_l^p\frac{\partial u_s^r}{\partial x_s} + a_7\beta_{1l}u_l^r\frac{\partial u_s^p}{\partial x_s}\\
&+ a_7\beta_{1s}\beta_{1l}u_l^r\frac{\partial u_s^r}{\partial x_s} + a_8u_s^p\frac{\partial u_l^p}{\partial x_l} + a_8\beta_{1l}u_s^p\frac{\partial u_l^r}{\partial x_l} + a_8\beta_{1s}u_s^r\frac{\partial u_l^p}{\partial x_l} + a_6u_l^p\frac{\partial u_l^p}{\partial x_l}\\
&+ a_8\beta_{1s}\beta_{1l}u_s^r\frac{\partial u_l^r}{\partial x_l} + a_6\beta_{1l}u_l^p\frac{\partial u_l^r}{\partial x_l} + a_6\beta_{1l}u_l^r\frac{\partial u_l^p}{\partial x_l} + a_6\beta_{1l}^2u_l^r\frac{\partial u_l^r}{\partial x_l} + a_5w_s^p\frac{\partial u_s^p}{\partial z^p}\\
&+ a_5a_9w_s^p\frac{\partial u_s^r}{\partial z_s^r} + \beta_{2s}\varepsilon_s^2w_s^r\frac{\partial u_s^p}{\partial z^p} + a_9\beta_{2s}\varepsilon_s^2w_s^r\frac{\partial u_s^r}{\partial z_s^r} + a_8w_l^p\frac{\partial u_s^p}{\partial z^p} + a_8a_9w_l^p\frac{\partial u_s^r}{\partial z_s^r}\\
&+ a_{13}\beta_{2l}w_l^r\frac{\partial u_s^p}{\partial z^p} + a_9\beta_{2l}w_l^r\frac{\partial u_s^r}{\partial z_s^r} + a_7w_s^p\frac{\partial u_l^p}{\partial z^p} + a_7a_{10}w_s^p\frac{\partial u_l^r}{\partial z_l^r} + a_{13}\beta_{2s}w_s^r\frac{\partial u_l^p}{\partial z^p}\\
&+ a_{10}a_{13}\beta_{2s}w_s^r\frac{\partial u_l^r}{\partial z_l^r} + a_6w_l^p\frac{\partial u_l^p}{\partial z^p} + a_6a_{10}w_l^p\frac{\partial u_l^r}{\partial z_l^r} + a_{14}w_l^r\frac{\partial u_l^p}{\partial z^p} + a_{10}a_{14}w_l^r\frac{\partial u_l^r}{\partial z_l^r}\\
&= -a_1\frac{\partial p_s^p}{\partial x_s} - a_2\frac{\partial p_l^p}{\partial x_l} - a_1\beta_{1s}^2\frac{\partial p_s^r}{\partial x_s} - a_2\beta_{1l}^2\frac{\partial p_l^r}{\partial x_l} + a_1\delta_s^2\frac{\partial^2u_s^p}{\partial x_s^2} + a_2\delta_l^2\frac{\partial^2u_l^p}{\partial x_l^2}\\
&+ a_1a_{15}\frac{\partial^2u_s^r}{\partial x_s^2} + a_2a_{16}\frac{\partial^2u_l^r}{\partial x_l^2} + a_{11}\frac{\partial^2u_s^p}{\partial z^{p2}} + a_{12}\frac{\partial^2u_l^p}{\partial z^{p2}} + a_1\beta_{1s}\frac{\partial^2u_s^r}{\partial z_s^{r2}} + a_2\beta_{1l}\frac{\partial^2u_l^r}{\partial z_l^{r2}},
\end{aligned} \tag{30}$$

$$\begin{aligned}
&a_{17}\frac{\partial w_s^p}{\partial t_s^p} + a_{18}\frac{\partial w_l^p}{\partial t_l^p} + a_1\beta_{2s}\frac{\partial w_s^r}{\partial t_s^r} + a_2\beta_{2l}\frac{\partial w_l^r}{\partial t_l^r} + a_{21}u_s^p\frac{\partial w_s^p}{\partial x_s} + \beta_{2s}a_5u_s^p\frac{\partial w_s^r}{\partial x_s}\\
&+ a_{21}\beta_{1s}u_s^r\frac{\partial w_s^p}{\partial x_s} + a_5\beta_{1s}\beta_{2s}u_s^r\frac{\partial w_s^r}{\partial x_s} + a_{17}\varepsilon_lu_l^p\frac{\partial w_s^p}{\partial x_s} + a_7\beta_{2s}u_l^p\frac{\partial w_s^r}{\partial x_s}\\
&+ a_{17}\beta_{1l}\varepsilon_lu_l^r\frac{\partial w_s^p}{\partial x_s}\\
&+ a_7\beta_{2s}\beta_{1l}u_l^r\frac{\partial w_s^r}{\partial x_s} + a_{18}\varepsilon_su_s^p\frac{\partial w_l^p}{\partial x_l} + a_8\beta_{2l}u_s^p\frac{\partial w_l^r}{\partial x_l} + a_{18}\beta_{1s}\varepsilon_su_s^r\frac{\partial w_l^p}{\partial x_l}\\
&+ a_8\beta_{1s}\beta_{2l}u_s^r\frac{\partial w_l^r}{\partial x_l}\\
&+ a_{22}u_l^p\frac{\partial w_l^p}{\partial x_l} + a_{18}\beta_{2l}u_l^p\frac{\partial w_l^r}{\partial x_l} + a_{22}\beta_{1l}u_l^r\frac{\partial w_l^p}{\partial x_l} + a_6\beta_{1l}\beta_{2l}u_l^r\frac{\partial w_l^r}{\partial x_l} + a_{21}w_s^p\frac{\partial w_s^p}{\partial z^p}\\
&+ a_5a_{19}w_s^p\frac{\partial w_s^r}{\partial z_s^r} + a_5\beta_{2s}w_s^r\frac{\partial w_s^p}{\partial z^p} + a_{19}\beta_{2s}\varepsilon_s^2w_s^r\frac{\partial w_s^r}{\partial z_s^r} + a_7\mu_lw_l^p\frac{\partial w_s^p}{\partial z^p}\\
&+ a_8a_{19}w_l^p\frac{\partial w_s^r}{\partial z_s^r}\\
&+ a_7\beta_{2l}w_l^r\frac{\partial w_s^p}{\partial z^p} + a_{13}a_{19}w_l^r\frac{\partial w_s^r}{\partial z_s^r} + a_7\mu_lw_s^p\frac{\partial w_l^p}{\partial z^p} + a_{20}a_7w_s^p\frac{\partial w_l^r}{\partial z_l^r}\\
&+ a_8\beta_{2l}w_l^r\frac{\partial w_l^p}{\partial z^p}\\
&+ a_{13}a_{20}\beta_{2s}w_s^r\frac{\partial w_l^r}{\partial z_l^r} + a_{22}w_l^p\frac{\partial w_l^p}{\partial z^p} + a_6a_{20}w_l^p\frac{\partial w_l^r}{\partial z_l^r} + a_6\beta_{2l}w_l^r\frac{\partial w_l^p}{\partial z^p}\\
&+ a_{20}\beta_{2l}\varepsilon_l^2w_l^r\frac{\partial w_l^r}{\partial z_l^r}\\
&= -\varepsilon_s\frac{\partial p_s^p}{\partial z^p} - \varepsilon_l\frac{\partial p_l^p}{\partial z^p} - a_9\beta_{1s}\varepsilon_s\frac{\partial p_s^r}{\partial z_s^r} - a_{10}\beta_{1l}\varepsilon_l\frac{\partial p_l^r}{\partial z_l^r} - 1 + a_{17}\delta_s^2\frac{\partial^2w_s^p}{\partial x_s^2}\\
&+ a_{18}\delta_l^2\frac{\partial^2w_l^p}{\partial x_l^2}\\
&+ a_1\beta_{2s}\delta_s^2\frac{\partial^2w_s^r}{\partial x_s^2} + a_2\beta_{2l}\delta_l^2\frac{\partial^2w_l^r}{\partial x_l^2} + \varepsilon_s\delta_s^2\frac{\partial^2w_s^p}{\partial z^{p2}} + \varepsilon_s\delta_l^2\frac{\partial^2w_l^p}{\partial z^{p2}} + a_1\beta_{2s}\frac{\partial^2w_s^r}{\partial z_s^{r2}}\\
&+ a_2\beta_{2l}\frac{\partial^2w_l^r}{\partial z_l^{r2}}.
\end{aligned} \tag{31}$$

where

$$\begin{aligned}
a_1 &= \mu_s\varepsilon_s, \quad a_2 = \mu_l\varepsilon_l, \quad a_3 = \frac{\beta_{2s}\varepsilon_s}{\delta_s^*}, \quad a_4 = \frac{\beta_{2l}\varepsilon_l}{\delta_l^*}, \quad a_5 = \mu_s\varepsilon_s^2,\\
a_6 &= \mu_l\varepsilon_l^2, \quad a_7 = \mu_s\varepsilon_s\varepsilon_l, \quad a_8 = \mu_l\varepsilon_s\varepsilon_l, \quad a_9 = \frac{\beta_{1s}}{\delta_s^*}, \quad a_{10} = \frac{\beta_{1l}}{\delta_l^*},\\
a_{11} &= \frac{\delta_s^2\varepsilon_s}{\mu_s}, \quad a_{12} = \frac{\delta_l^2\varepsilon_l}{\mu_l}, \quad a_{13} = \varepsilon_s\varepsilon_l, \quad a_{14} = \beta_{2l}\varepsilon_l^2, \quad a_{15} = \beta_{1s}\delta_s^2,\\
a_{16} &= \beta_{1l}\delta_l^2, \quad a_{17} = \mu_s^2\varepsilon_s, \quad a_{18} = \mu_l^2\varepsilon_l, \quad a_{19} = \frac{\beta_{2s}}{\delta_s^*}, \quad a_{20} = \frac{\beta_{2l}}{\delta_l^*}\\
a_{21} &= \mu_s^2\varepsilon_s^2, \quad a_{22} = \mu_l^2\varepsilon_l^2
\end{aligned}$$

4.1. The estimation of the order of magnitude for the small parameters

The governing equations have ten small parameters which are :μ_s, μ_l, β_{1s}, β_{1l}, β_{2s}, β_{2l}, ϵ_s, ϵ_l, δ_s, and δ_l. We attempt to find approximate relations to group these parameters together and thus decreasing their number. First, we note that the parameters β_{1s} and β_{1l} are multiplied by the bottom velocity to represent the friction velocities as in single wave motion. Therefore, by comparing the friction factors of these two motions, the relative order of magnitude of the parameters, β_{1s} and β_{1l}, can be estimated as $O(\beta_{1l}/\beta_{1s}) \approx O(R_{es}/R_{el})$.

Here, the Reynolds number is given as $R_e = u_b^2/\omega\nu$, where the expression for the maximum particle excursion is used. After using the maximum bottom velocity expressions for the two motions and performing simple manipulations, the following relations are obtained:

$$\begin{aligned} O(R_{es}/R_{el}) &= O(\varepsilon_s^2\mu_l/\varepsilon_l^2\mu_s). \\ O(\beta_{1l}) &\approx O\left(\beta_{1s}/\mu_s^{(m-1)/4}\sqrt{\frac{\epsilon_s}{\epsilon_l}}\right). \end{aligned} \tag{32}$$

Second, it is presumed that the dispersion parameter of the shorter wave and the longer wave can be related as $O(\mu_l) = O(\mu_s^m)$, where m is a free power that depends on the characteristics of the problem. Third, it is assumed that the two waves have comparable amplitude, $O(\epsilon_s) \approx O(\epsilon_l)$. Therefore, the Reynolds number of the shorter wave is smaller than the Reynolds number of the longer wave, $O(R_{es}) \leq O(R_{el})$. Thus, the friction factor of the longer wave is smaller than the friction factor of the shorter wave ($f_{wl} \leq f_{ws}$), and the parameter β_1 of the longer wave is smaller than β_1 of the shorter wave. This leads to ($\beta_{1l} \leq \beta_{1s}$). By substituting the previous relations into the governing equations, the number of small parameters are reduced to eight: β_{1s}, β_{2s}, β_{2l}, μ_s, ϵ_s, ϵ_l, δ_s, and δ_l.

Finally, it is assumed that, $O(\beta_{2s}) = O(\beta_{1s}\delta_s^*\mu_s)$ and, $O(\beta_{2l}) = O(\beta_{1l}\delta_l^*\mu_l)$, as it is done in the single motion. Therefore, it is possible to reduce the number of small parameters to six. Finally, each wave motion is assumed to follow the Boussinesq assumption. Thus, $O(\varepsilon_s) \approx O(\mu_s^2) \ll 1$, and the same for the longer motion, $O(\varepsilon_l) \approx O(\mu_l^2) \ll 1$. By applying this final assumption, the number of the free parameters is decreased to four.

4.2. Model results

The bottom boundary layers generated under the interaction of short and long waves with different long wave forcings are investigated in this section. The first interaction type consists of two periodic short and long waves. The second interaction type consists of short waves interacting with a solitary wave. The first case represents periodic forcing whereas the second case represents transient forcing. The boundary layer response under these two different forcings is discussed.

4.3. Two oscillatory motions

In this section, the bottom boundary layer generated under two interacting oscillatory wave motions is presented. The parameters of the problem are: $\varepsilon_s = 0.05$, $\varepsilon_l = 0.005$, $\mu_s = 0.12$, $\mu_l = 0.04$, and thus $m \approx 1.5$. The Reynolds number and the friction factor are calculated and $O(\beta_{1s}) \approx O(0.01)$. It is assumed that $O(\delta_s^*) \approx O(\varepsilon_s)$ and $O(\delta_l^*) \approx O(\beta_{1s})$. After applying these relations and keeping only the leading order terms, the dimensional governing equations are,

$$\frac{\partial u_s^p}{\partial x_s} + \frac{\partial w_s^p}{\partial z^p} + \frac{\partial u_l^p}{\partial x_l} + \frac{\partial w_l^p}{\partial z^p} + \frac{\partial u_s^r}{\partial x_s} + \frac{\partial w_s^r}{\partial z_s^r} + \frac{\partial u_l^r}{\partial x_l} + \frac{\partial w_l^r}{\partial z_l^r} = 0, \tag{33}$$

$$\begin{aligned} &\frac{\partial u_s^p}{\partial t_s^p} + \frac{\partial u_l^p}{\partial t_l^p} + \frac{\partial u_s^r}{\partial t_s^r} + \frac{\partial u_l^r}{\partial t_l^r} + u_s^p\frac{\partial u_s^p}{\partial x_s} + w_s^p\frac{\partial u_s^r}{\partial z_s^r} + w_s^p\frac{\partial u_s^p}{\partial z^p} + u_l^p\frac{\partial u_s^p}{\partial x_s} \\ &\quad + w_s^p\frac{\partial u_l^p}{\partial z^p} + w_s^p\frac{\partial u_l^r}{\partial z_l^r} = -\frac{1}{\rho}\frac{\partial p_s^p}{\partial x_s} - \frac{1}{\rho}\frac{\partial p_l^p}{\partial x_l} + \frac{\partial^2 u_s^r}{\partial z_s^{r2}} + \frac{\partial^2 u_l^r}{\partial z_l^{r2}}, \end{aligned} \tag{34}$$

$$\frac{\partial w_s^p}{\partial t_s^p} + u_s^p\frac{\partial u_s^p}{\partial x_s} + w_s^p\frac{\partial w_s^p}{\partial z^p} + \frac{1}{\rho}\frac{\partial p_s^p}{\partial z^p} + \frac{1}{\rho}\frac{\partial p_l^p}{\partial z^p} + g = 0. \tag{35}$$

The equations contain the potential component terms of both the short and the long waves. The remaining terms are for the rotational component along with some interaction terms of the potential and rotational components. After factoring out the potential solution, the dimensional governing equations for the rotational component are,

$$\frac{\partial u_s^r}{\partial x_s} + \frac{\partial w_s^r}{\partial z_s^r} + \frac{\partial u_l^r}{\partial x_l} + \frac{\partial w_l^r}{\partial z_l^r} = 0, \tag{36}$$

$$\frac{\partial u_s^r}{\partial t_s^r} + \frac{\partial u_l^r}{\partial t_l^r} + w_s^p\frac{\partial u_s^r}{\partial z_s^r} + w_s^p\frac{\partial u_l^r}{\partial z_l^r} = \frac{\partial^2 u_s^r}{\partial z_s^{r2}} + \frac{\partial^2 u_l^r}{\partial z_l^{r2}}. \tag{37}$$

Two boundary conditions are required in order to solve the equations: the velocity gradient at the top boundary and the bottom velocity. The shorter wave motion is superimposed on an existing longer wave in this study. Therefore, the combined potential of the short and the long wave is the forcing mechanism. The bottom boundary condition is taken to satisfy the no-slip boundary condition, and zero shear stress is assumed at the water surface,

$$u_t^r = -u_t^p \quad \text{at} \quad z = -h, \tag{38}$$

$$\frac{\partial u_t^r}{\partial z^r} = 0 \quad \text{at} \quad z = \eta, \tag{39}$$

where u_t^r is the total rotational horizontal velocity and u_t^p is the total potential horizontal velocity.

The computational domain length is chosen to be 50 wavelengths of the longer wave. The simulation is run for 80 wave periods of the longer wave to ensure a fully developed boundary layer. The computational domain has $\Delta x = 0.03\ m$, $\Delta z = 0.00001\ m$, and $\Delta t = 0.0005\ s$ with 0.5 m water depth. Sponge layers are used on the left and right boundaries to absorb the wave energy. The two oscillatory waves are generated using the source function as described in Wei and Kirby (1995) inside the one-dimensional Boussinesq-type wave model. The potential velocities of the short wave and the long wave are passed to the viscous-sigma-model. The viscous-sigma-model solves the Eqs. (36) and (37) with the two boundary conditions (38) and (39), to obtain the vertical profile of the combined rotational velocity.

Two different simulations are presented in this section. In the first simulation, the effect of the coupling term under the interaction of two waves is quantified. The potential forcing is fixed and the horizontal momentum equation is solved twice: one time with the coupling terms, (the third and fourth terms in the Eq. (37, nonlinear model solution) , and a second time without the coupling terms (linear model solution). The combined velocity profile at different locations are shown in Fig. (7), where $u^\alpha = u/\sqrt{gh}$, $\eta^* = \eta/h$, and $z^* = z/h$. It is noticed that the boundary layer response is different in these two cases despite the same potential forcing. The nonlinear model solution is larger in the accelerating phase while the linear model solution is larger in the decelerating phase. Thus, the superposition principle should be used carefully while studying bottom boundary layer and sediment transports under wave interacting. Also, we expect the flow outside the boundary layer to be reasonably well captured using the Boussinesq model and under the linear forcing in this case and hence the comparison for the flow outside the boundary won't be presented here.

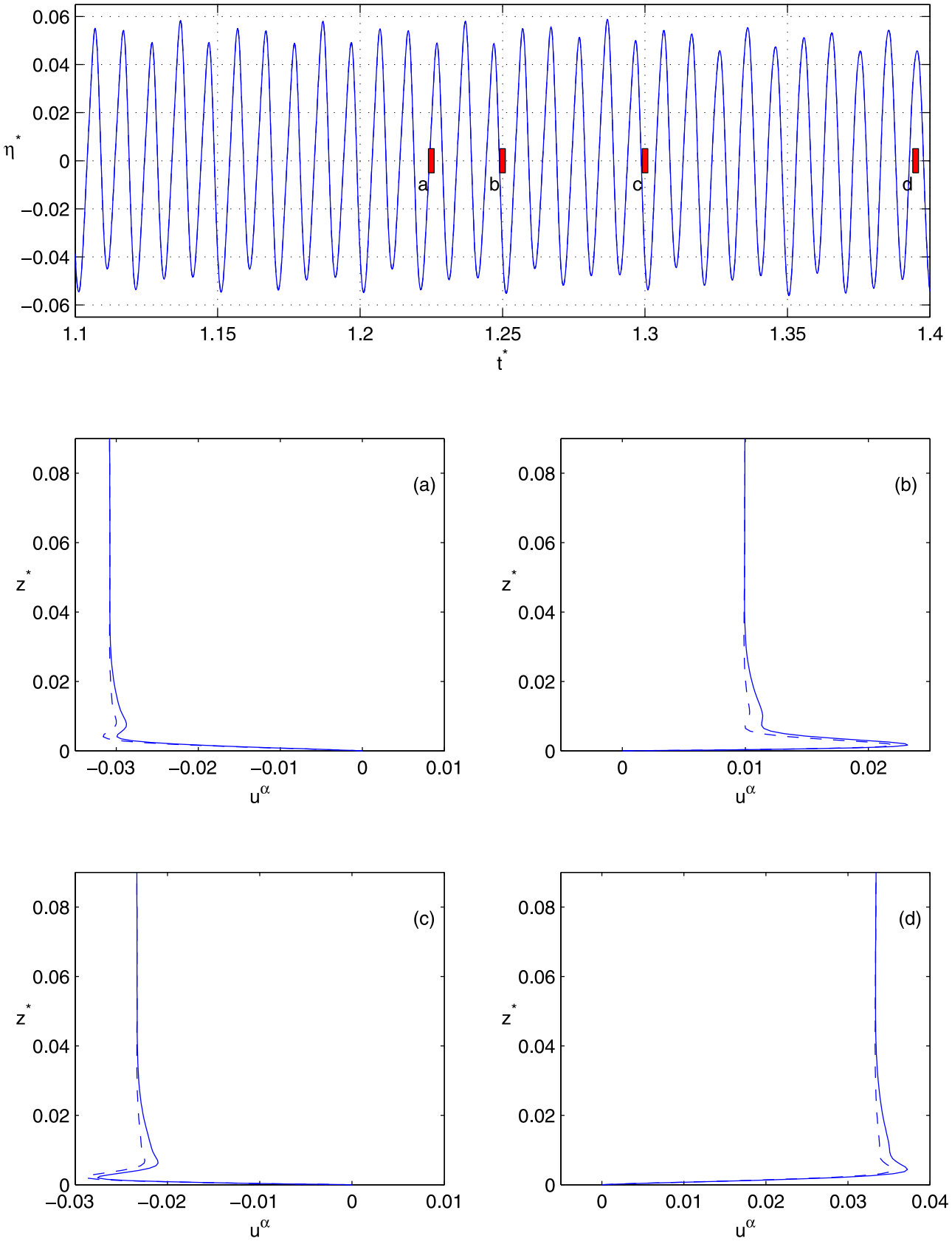

Fig. 7. Surface elevations and vertical profiles of the horizontal velocity in the laminar boundary layer under the interaction of two oscillatory motions at different times of the same potential forcing. Solid line: nonlinear solution; dashed line: linear solution.

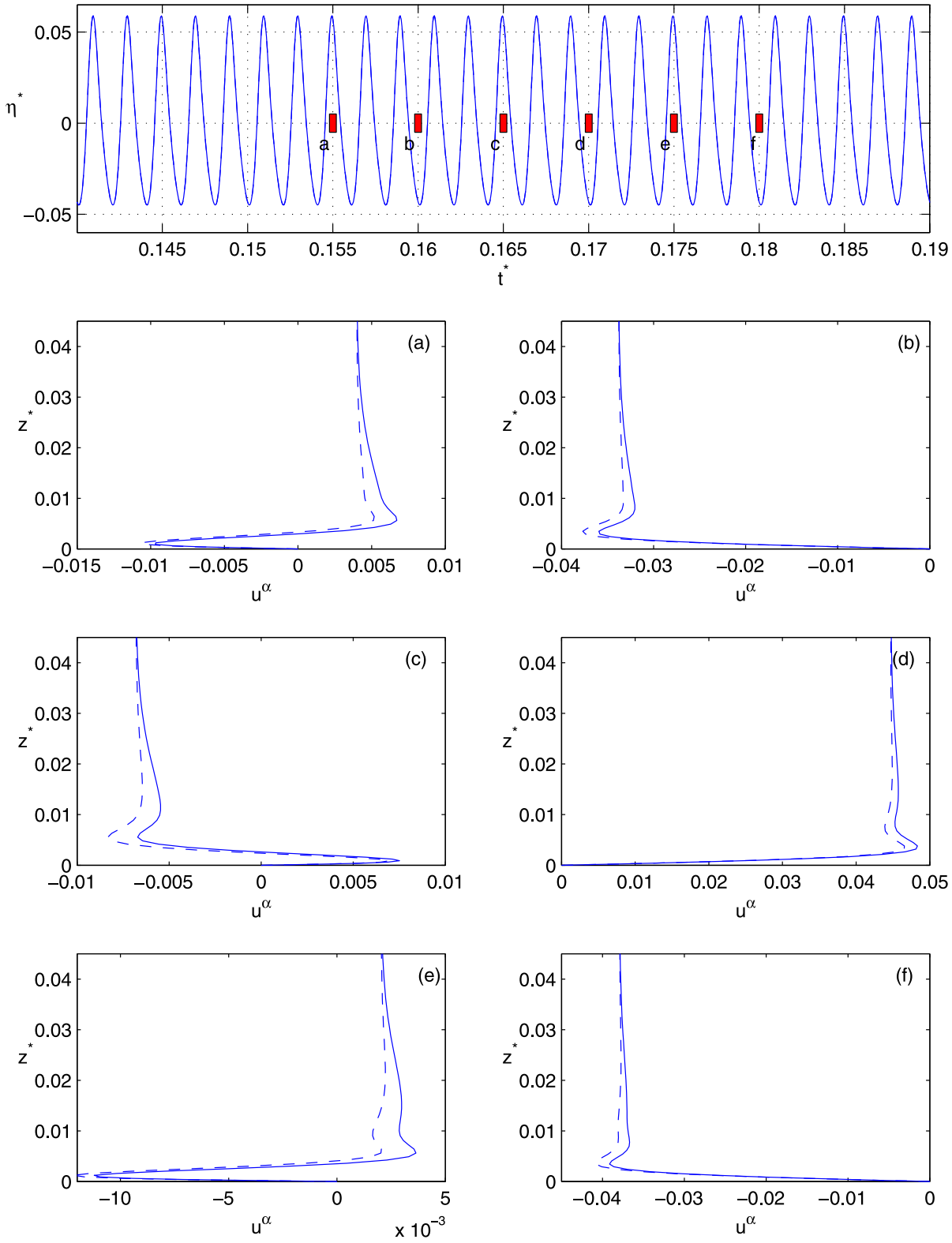

Fig. 8. Surface elevations and vertical profile of the horizontal velocity in the laminar boundary layer under the interaction of a solitary wave and swell waves at different times of the same potential forcing. Solid line: nonlinear solution; dashed line: linear solution.

4.4. Periodic waves over solitary wave

In this simulation, the bottom boundary layer is forced by the interaction of a solitary wave and short periodic waves. The short waves are generated in the Boussinesq numerical wave model using the source function. The initial location of the solitary wave is set behind the source location. The characteristics of the short wave are as before (ε_s = 0.05 and μ_s=0.12) and the solitary wave has ε_l = 0.005. The differences in the velocity profile in this test case are more pronounced as compared to the difference seen in the two oscillatory motions, as shown in Fig. (8). Moreover, the combined velocity profiles show inflection points in the accelerating phase. This remark does not exist in

the velocity profile under a single solitary wave. An explanation for this remark could be to the rapid acceleration and deceleration phases of the solitary wave compared to those of the oscillatory long wave. Also, the effect of the solitary wave is found in the boundary layer even after it passes, see Fig. (8)f.

5. Conclusions

This work aims to incorporate bottom boundary layer effects forced by a single wave and under two interacting waves. The multiple-scale approach is applied to the Navier–Stokes equations where the fluid velocities and pressure are decomposed into two components: potential and rotational. Both components are allowed to coexist in the entire water column. Different time scales are employed for the two components: a convective time scale is used for the potential component and a viscous time scale for the rotational component. The friction velocity is used to scale the rotational velocity component; it is represented here as a small parameter β_1 multiplied by the bottom velocity u_b , i.e., $u_* = \beta_1 u_b$. The order of magnitude of the coefficient, β_1, is found from the analysis and is related to the friction factor, which depends on the characteristics of the problem under consideration.

By applying this approach, a set of equations for the rotational velocity component are derived. The boundary layer thickness is not assumed to be finite, and therefore it is not necessary to use different models to solve for the flow kinematics inside and outside the boundary layer. A one-dimensional numerical model with σ-coordinate transformation in the vertical direction is used. The single wave forcing consists of harmonic forcing (e.g. oscillatory wave) and transient forcing (e.g. solitary wave). Linear wave theory is used to obtain the potential velocity component for the oscillatory wave motion case, while a one-dimensional Boussinesq-type equation is solved numerically to obtain the potential velocity component in the solitary wave motion case.

A one way-coupling is used where the potential horizontal bottom velocity and the vertical component of the potential velocity are passed to the viscous-sigma-model to solve for the rotational velocity component. Finally, the two components (potential and rotational) are summed to obtain the total velocity field. The order of magnitude analysis shows that the leading-order coupling between the potential and rotational components occurs through the vertical convective acceleration term, $w^P(\partial u^r/\partial z)$. The model results agree well with the available experimental data and the numerical solutions for different forcing conditions, with better matching when including the coupling term under the various wave forcings.

Under solitary waves, the bottom shear stress undergoes a change in sign during the wave cycle, although the velocity outside the boundary layer is always positive in the direction of wave propagation. The conventional way of calculating bottom shear stresses (i.e. the quadratic law using the bottom velocity), will not be able to predict this change in sign. In the approach outlined in this paper, the bottom shear stress is calculated using the rotational velocity gradient at the bottom, and the sign change is captured.

For the two wave motion cases, the governing equations for the bottom boundary layer forced by the interaction of two distinct wave motions are derived. Both motions (the shorter and the longer waves) are decomposed into two components (potential and rotational). Laminar boundary layer approximations are used to reduce the number of small parameters that appear in the governing equations. Different examples of the boundary layer under two wave motions are presented here: 1) the interaction of long and short oscillatory wave motions and 2) the interaction of a solitary wave with periodic waves. The analysis of the two wave motions indicates that nonlinear effects in the rotational solution may be significant even when nonlinear effects in the potential forcing are negligible. These results suggest the careful use of the superposition principle in case of interacting two wave motions.

References

Blondeaux, P., Vittori, G., 2012. Rans modelling of the turbulent boundary layer under a solitary wave. Coastal Eng. 60 (1), 1–10.

Cox, D., Kobayashi, N., Okayasu, A., 1996. Bottom shear stress in the surf zone. J. Geophys. Res. 101 (C6), 14337–14348.

van Doorn, T., 1981. Experimental investigation of near-bottom velocities in water waves without and with a current: report on investigations. Technical Report. Waterloopkundig Laboratorium, Delft Hydraulics Laboratory.

Gilbert, R., Zedler, E., Grilli, S., Street, R., 2007. Progress on nonlinear-wave-forced sediment transport simulation. IEEE J. Oceanic Eng. 32 (1), 236–248.

Harris, J., Grilli, S., 2012. A perturbation approach to large eddy simulation of wave-induced bottom boundary layer flows. Int. J. Numer Methods Fluids 68 (12), 1574–1604.

Jensen, B., Sumer, B., Fredsoe, J., 1989. Turbulent oscillatory boundary layers at high reynolds numbers. J. Fluid Mech. 206, 265–297.

Jonsson, I.G., Carlsen, N.A., 1976. Experimental and theoretical investigations in an oscillatory turbulent boundary layer. J. Hydraul. Res. 14 (1), 45–60.

Kamphuis, J., 1975. Friction factor under oscillatory waves. Am. Soc. Civil Eng. 101 (2), 135–144.

Kim, D.-H., Lynett, P.J., Socolofsky, S.A., 2009. A depth-integrated model for weakly dispersive, turbulent, and rotational fluid flows. Ocean Modell. 27 (3–4), 198–214.

Lamb, S.H., 1932. Hydrodynamics. Cambridge University Press.

Lee, S.-K., Cheung, K.F., 1999. Laminar and turbulent bottom boundary layer induced by nonlinear water waves. J. Hydraul. Eng. 125 (6), 631–644.

Lin, P., Zhang, W., 2008. Numerical simulation of wave-induced laminar boundary layers. Coastal Eng. 55 (5), 400–408.

Liu, P.-F., 2006. Turbulent boundary-layer effects on transient wave propagation in shallow water. Proc. R. Soc. London, Ser. A 462 (2075), 3481–3491.

Liu, P.-F., Park, Y.S., Cowen, E., 2007. Boundary layer flow and bed shear stress under a solitary wave. J. Fluid Mech. 574, 449–463.

Liu, P.L.-F., Orfila, A., 2004. Viscous effects on transient long-wave propagation. J. Fluid Mech. 520, 83–92.

Lynett, P., Liu, P.-F., 2002. A numerical study of submarine-landslide-generated waves and run-up. Proc. R. Soc. London, Ser. A 458 (2028), 2885–2910.

Mirfenderesk, H., Young, I.R., 2003. Direct measurements of the bottom friction factor beneath surface gravity waves. Appl. Ocean Res. 25 (5), 269–287.

Nielsen, P., 1992. Coastal Bottom Boundary Layers and Sediment Transport. World Scientific.

Nwogu, O., 1993. Alternative form of Boussinesq equations for Nearshore Wave Propagation. J. Waterw., Port, Coastal, Ocean Eng. 119, 618–638.

Orfila, A., Simarro, G., Liu, P., 2007. Bottom friction and its effects on periodic long wave propagation. Coastal Eng. 54 (11), 856–864.

Park, Y., 2009. Seabed dynamics and breaking waves. Cornell University Ph.D. thesis.

Riedel, H.P., Kamphuis, J.W., Brebner, A., 1972. Measurement of bed shear stress under waves. Proc. 13th Conf. Coastal Engrg., Chapter 31, Am. Soc. Civ. Engres., New York 1, 587–603.

Sleath, J., 1987. Turbulent oscillatory flow over rough beds. J. Fluid Mech. 182, 369–409.

Vittori, G., Blondeaux, P., 2008. Turbulent boundary layer under a solitary wave. J. Fluid Mech. 615, 433–443.

Wei, G., Kirby, J.T., 1995. Time-dependent numerical code for extended boussinesq equations. J. Waterway, Port, Coastal Ocean Eng. 121 (5), 251–261.

Zang, Y., Street, R., Koseff, J., 1994. A non-staggered grid, fractional step method for time-dependent incompressible navier-stokes equations in curvilinear coordinates. J. Comput. Phys. 114 (1), 18–33.